

# A nanoenzyme-modified hydrogel targets macrophage reprogramming-angiogenesis crosstalk to boost diabetic wound repair

Shan He<sup>a,b,1</sup>, Zhenhao Li<sup>c,1</sup>, Lu Wang<sup>a</sup>, Nannan Yao<sup>d</sup>, Huangding Wen<sup>b</sup>, Huageng Yuan<sup>a</sup>, Jiatao Zhang<sup>e,\*\*\*</sup>, Zhiqing Li<sup>b,\*\*</sup>, Chuanan Shen<sup>a,\*</sup>

<sup>a</sup> Department of Burns and Plastic Surgery, Fourth Medical Center of PLA General Hospital, No. 51, Fucheng Road, Haidian District, Beijing, 100048, China

<sup>b</sup> Department of Burns, Nanfang Hospital, Southern Medical University, Guangzhou, 510515, China

<sup>c</sup> Department of General Surgery, Nanfang Hospital, The First School of Clinical Medicine, Southern Medical University, Guangzhou, 510515, China

<sup>d</sup> Department of Neurology, Cangzhou Central Hospital, Cangzhou, 061000, China

<sup>e</sup> Jiatao Zhang, Key Laboratory of Medical Molecule Science and Pharmaceutical Engineering, Ministry of Industry and Information Technology, Beijing Key Laboratory of Construction Tailorable Advanced Functional Materials and Green Applications, School of Chemistry and Chemical Engineering, Beijing Institute of Technology, Beijing, 100081, China

## ARTICLE INFO

### Keywords:

Diabetic wound  
Nanoenzyme  
Macrophages polarization  
NLRP3  
Hydrogel

## ABSTRACT

Diabetic wounds has a gradually increasing incidence and morbidity. Excessive inflammation due to immune imbalance leads to delayed wound healing. Here, we reveal the interconnection between activation of the NLRP3 inflammatory pathway in endotheliocyte and polarization of macrophages via the cGAS-STING pathway in the oxidative microenvironment. To enhance the immune-regulation based on repairing mitochondrial oxidative damage, a zeolitic imidazolate framework-8 coated with cerium dioxide that carries Rho-associated protein kinase inhibition Y-27632 (CeO<sub>2</sub>-Y@ZIF-8) is developed. It is encapsulated in a photocross-linkable hydrogel (GelMA) with cationic quaternary ammonium salt groups modified to endow the antibacterial properties (CeO<sub>2</sub>-Y@ZIF-8@Gel). CeO<sub>2</sub> with superoxide dismutase and catalase activities can remove excess reactive oxygen species to limit mitochondrial damage and Y-27632 can repair damaged mitochondrial DNA, thus improving the proliferation of endotheliocyte. After endotheliocyte uptakes CeO<sub>2</sub>-Y@ZIF-8 NPs to degrade peroxides into water and oxygen in cells and mitochondria, NLRP3 inflammatory pathway is inhibited and the leakage of oxidatively damaged mitochondrial DNA (Ox-mtDNA, a damage-associated molecular pattern) through mPTP decreases. Furthermore, as the cGAS-STING pathway activated by Ox-mtDNA down-regulated, the M2 phenotype polarization and anti-inflammatory factors increase. Collectively, CeO<sub>2</sub>-Y@ZIF-8@Gel, through remodeling the crosstalk between macrophage reprogramming and angiogenesis to alleviate inflammation in the microenvironment and accelerates wound healing.

## 1. Introduction

The global prevalence of diabetes in adults is expected to rise to 7.7 % in 2023. The complications of diabetes jeopardize both physical and psychological well-being of the patients, resulting in undermined quality of life and increased medical burden [1]. Diabetic wounds (DW) features persistent hyperglycemia causing local microenvironmental imbalance, often accompanied by impaired vascularization of basal

granulation tissue, and eventually refractory ulcer would develop [2]. Specifically, the continuous inflammatory and high-glucose microenvironment produces large amounts of reactive oxygen species (ROS), and the high expression of ROS can cause damage to cells and tissues [3]. It is estimated that DW is responsible for about 60 % of amputations, which is the main reason for diabetic patients to be hospitalized [4]. Therefore, to orchestrate an effective angiogenic therapeutic strategy to clear excessive ROS and improve the microenvironment of DW is urgently

Peer review under responsibility of KeAi Communications Co., Ltd.

\* Corresponding author.

\*\* Corresponding author.

\*\*\* Corresponding author.

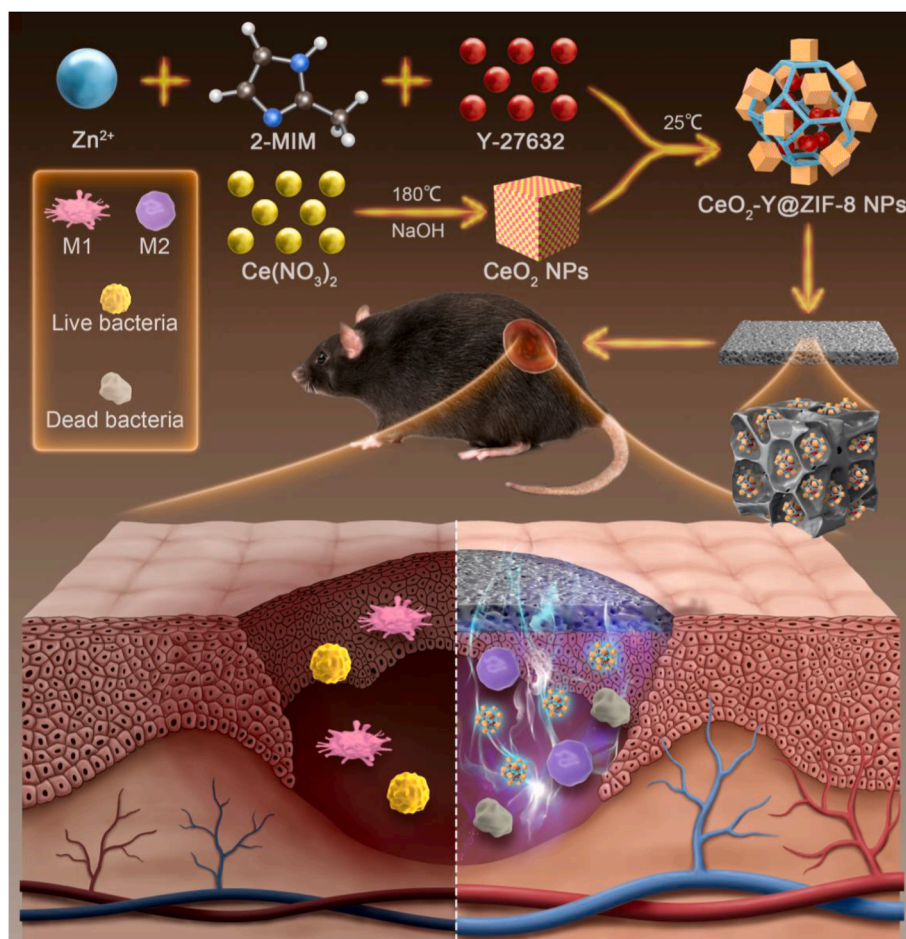
E-mail addresses: [zhangjt@bit.edu.cn](mailto:zhangjt@bit.edu.cn) (J. Zhang), [lizq@smu.edu.cn](mailto:lizq@smu.edu.cn) (Z. Li), [shenchuanan@301hospital.com.cn](mailto:shenchuanan@301hospital.com.cn) (C. Shen).

<sup>1</sup> S.H. and Z.L. contributed equally to this article.

<https://doi.org/10.1016/j.bioactmat.2024.01.005>

Received 8 December 2023; Received in revised form 27 December 2023; Accepted 5 January 2024

2452-199X/© 2024 The Authors. Publishing services by Elsevier B.V. on behalf of KeAi Communications Co. Ltd. This is an open access article under the CC BY-NC-ND license (<http://creativecommons.org/licenses/by-nc-nd/4.0/>).



**Scheme 1.** Schematic of the structural units and fabrication process of  $\text{CeO}_2\text{-Y@ZIF-8@Gel}$ , and the mechanism of the treatment for infected diabetic wounds.

needed.

In recent years, there has been increasing evidence that mitochondrial dysfunction can be a barrier in DW healing. First, the accumulation of reactive oxygen species (ROS) from oxidative stress inside the mitochondria in endothelial cells activate the nucleotide-binding and oligomerization (NACHT) domain, leucine-rich repeat (LRR), and pyrin domain (PYD)-containing protein 3 (NLRP3) to trigger NLRP3 inflammasome assembly [5,6]. Notably, a NLRP3-mediated inflammatory cascade has been implicated in deficiencies in angiogenesis and ulcer healing in diabetic patients [7]. As NLRP3 activates caspase-1, which then cleaves inactive pro-interleukin-1 $\beta$  to the bioactive forms, inflammation caused can reduce insulin sensitivity as well as damage vascular endothelial cells [8]. Second, both lipopolysaccharides (LPS) derived from microbes or immunogenic interferons released from dead endothelial cells would impact on macrophages significantly in chronic wound. In detail, Conversion of M2 to M1 M $\Phi$ s produces inflammation to increase in a hyperglycemia micro-environment characterized by oxidative stress, proteolysis, and cellular damage [9]. Third, the extracellular release of oxidatively damaged mitochondrial DNA (Ox-mtDNA) would be engulfed by macrophages [10,11]. DNA-sensing enzyme cyclic GMP-AMP (cGAMP) synthase (cGAS) activates the stimulator of interferon genes (STING) and production of type I interferons (IFN), soon afterwards macrophages transform into M1 and the inflammatory response amplifies [12–14]. Therefore, alleviating the inflammatory response in the microenvironment through recover the physiological status of endothelial cells and controlling microbial infection to reduce NLRP3 in cells and guides macrophage polarization is crucial in promoting diabetic wound healing.

Nanotechnology-mediated antioxidative therapy has been proven a

promising method for the treatment of oxidative damage-induced diseases. Here, we report a wound-friendly and degradable scaffold ( $\text{CeO}_2\text{-Y@ZIF-8@Gel}$ ) fabricated by encapsulating  $\text{CeO}_2\text{-Y@ZIF-8}$  into a photo-crosslinked gelatin methacryloyl (GelMA) hydrogels. Zeolitic imidazolate framework-8 (ZIF-8) nanoparticle (NP) binds cerium dioxide ( $\text{CeO}_2$ ) which consumes and reduces ROS to its surface at multiple sites, and encapsulates the Rho-associated coiled-coil forming protein kinase (ROCK) inhibitor Y-27632 [(R)-(+)-trans-4-(1-Aminoethyl)-N-(4-pyridyl) cyclohexane carboxamide dihydrochloride] which repairs mitochondrial damage and reduces cell apoptosis [15].  $\text{CeO}_2$  could modify the surface properties of ZIF-8 NPs and prevent aggregation, thus enhancing the stability of  $\text{CeO}_2\text{-Y@ZIF-8}$  under physiological conditions. Moreover, the cavity and porous structure could endow the materials with strong size-sieving ability to regulate the diffusion and reaction process. Benefiting from the cross-linked cationic quaternary ammonium salt (QAS),  $\text{CeO}_2\text{-Y@ZIF-8@Gel}$  exhibits antimicrobial activity [16]. Subsequently, the less leakage of Ox-mtDNA reduces cGAS-STING activation and cGAS-STING-mediated M1 polarization. The increased M2 secrete more anti-inflammatory cytokines and trophic factors, achieving a self-regulated immune balance to promote the regeneration and vascularization of the diabetic wound as shown in [Scheme 1](#).  $\text{CeO}_2\text{-Y@ZIF-8@Gel}$ , as a versatile dressing integrating antibacterial, anti-inflammatory and wound adaptability, showing a great potential in rapid repair of DW through regulating the macrophage-endotheliocyte crosstalk in the oxidative microenvironment.

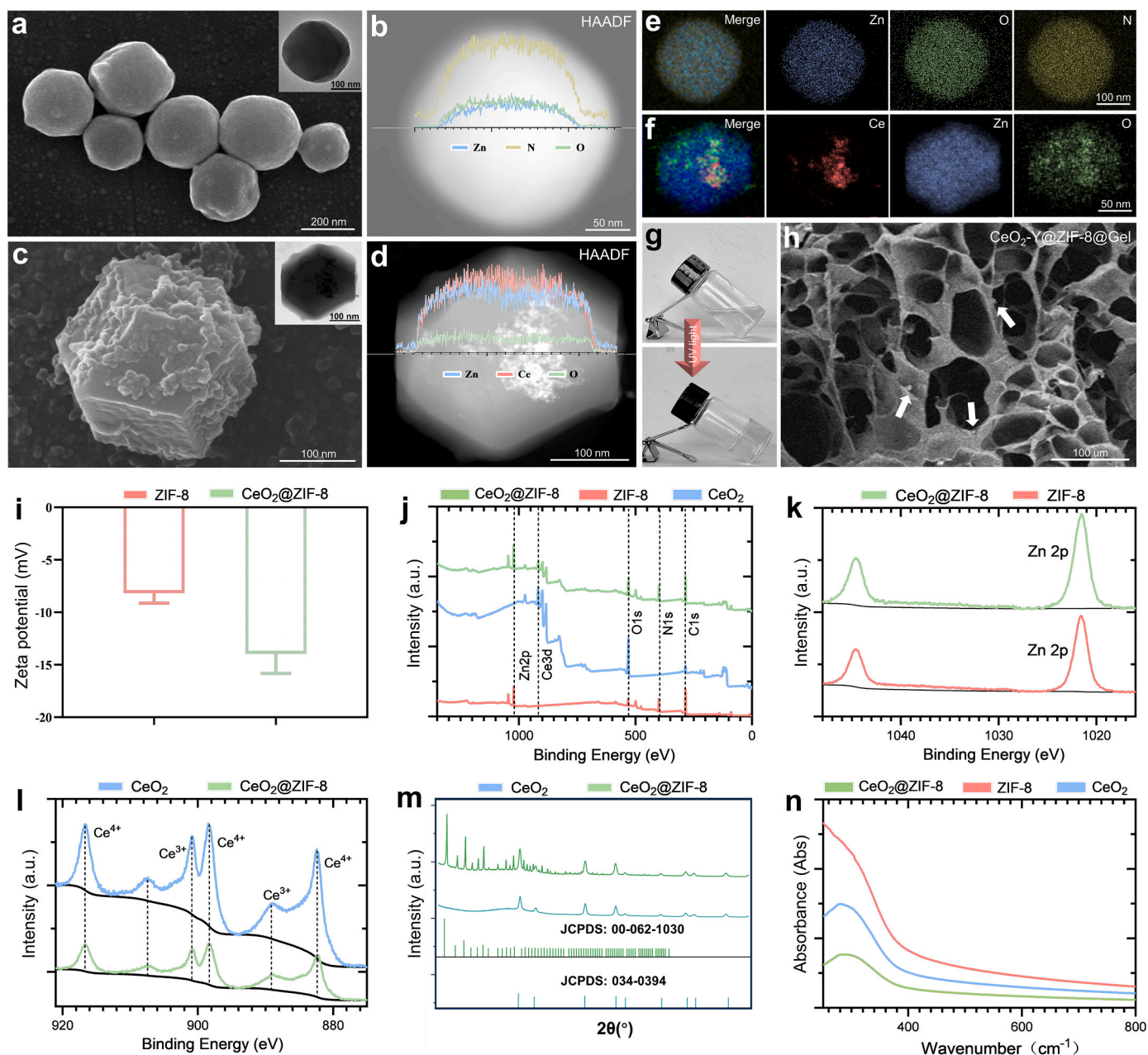


**Fig. 1.** Preparation and characterization of multi-enzymic nanoplatform  $\text{CeO}_2\text{-Y@ZIF-8@Gel}$ . (a) Scanning electron microscopy (SEM) and transmission electron microscopy (TEM) depictions of ZIF-8. (b) A high-angle annular dark-field imaging-scanning TEM (HAADF-STEM) rendition and a correlated TEM-energy-dispersive x-ray spectroscopy (TEM-EDS) representation of ZIF-8. (c) SEM and TEM visualizations of the  $\text{CeO}_2\text{@ZIF-8}$  nanocomposite. (d) HAADF-STEM portrayal and aligned TEM-EDS depiction of  $\text{CeO}_2\text{@ZIF-8}$ . Elemental distributions for (e) ZIF-8 NP and (f)  $\text{CeO}_2\text{@ZIF-8}$ . (g) Representative SEM image of  $\text{CeO}_2\text{-Y@ZIF-8@Gel}$ . (h) Photographic evidence of Gelma post-ultraviolet (UV) light exposure supplemented with photoinitiators. (i) Zeta potential evaluations of ZIF-8 and  $\text{CeO}_2\text{-Y@ZIF-8}$ . (j) X-ray photoelectron spectroscopy (XPS) profiles of  $\text{CeO}_2$ , ZIF-8, and  $\text{CeO}_2\text{@ZIF-8}$ . (k) Precision XPS interrogation of Zn 2p. (l) Detailed XPS analyses of Ce 3d. (m) X-ray diffraction (XRD) delineations for  $\text{CeO}_2$  and  $\text{CeO}_2\text{@ZIF-8}$ . (n) Ultraviolet-visible (UV-Vis) spectral comparisons of  $\text{CeO}_2$ , ZIF-8, and  $\text{CeO}_2\text{@ZIF-8}$ .

## 2. Results

### 2.1. Fabrication and characterization of $\text{CeO}_2\text{-Y@ZIF-8@Gel}$

For the fabrication of  $\text{CeO}_2\text{-Y@ZIF-8@Gel}$ , we initially synthesized zeolitic imidazolate framework-8 (ZIF-8)-encapsulated cerium dioxide nanoparticles ( $\text{CeO}_2$  NPs). By subsequently incorporating Y-27632, we obtained  $\text{CeO}_2\text{-Y@ZIF-8}$  NPs, as illustrated in Fig. 1a. This methodology was strategically chosen to augment both catalytic and antioxidative functionalities. In the devised nanosystem, ZIF-8 NPs were synthesized through the coordination of metallic  $\text{Zn}^{2+}$  ions with 2-methylimidazole

in a methanolic milieu. The resultant ZIF-8 particles, manifesting a diameter close to 245 nm, were derived in accordance with conventional methodologies. As illustrated in Fig. 1b and e, element mapping further corroborated the efficacious integration of  $\text{Zn}^{2+}$  ions into the ZIF-8 NPs structure.  $\text{CeO}_2$  NPs with a size of  $\sim 12 \pm 5$  nm were successfully created through a facile hydrothermal method (Figs. S1 and S2, Supporting Information). Here, Y-27632, a Rho-associated protein kinase (ROCK) inhibitor targeting lysosomes in mitochondria to and removing of damaged mitochondria from cells, was grafted onto the surfaces of the  $\text{CeO}_2\text{-PVP}$  NPs to form  $\text{CeO}_2\text{-Y-27632}$  NPs ( $\text{CeO}_2\text{-Y}$  NPs). Further, we also created the nanocomposite of  $\text{CeO}_2\text{-Y@ZIF-8}$  where the  $\text{CeO}_2\text{-Y}$

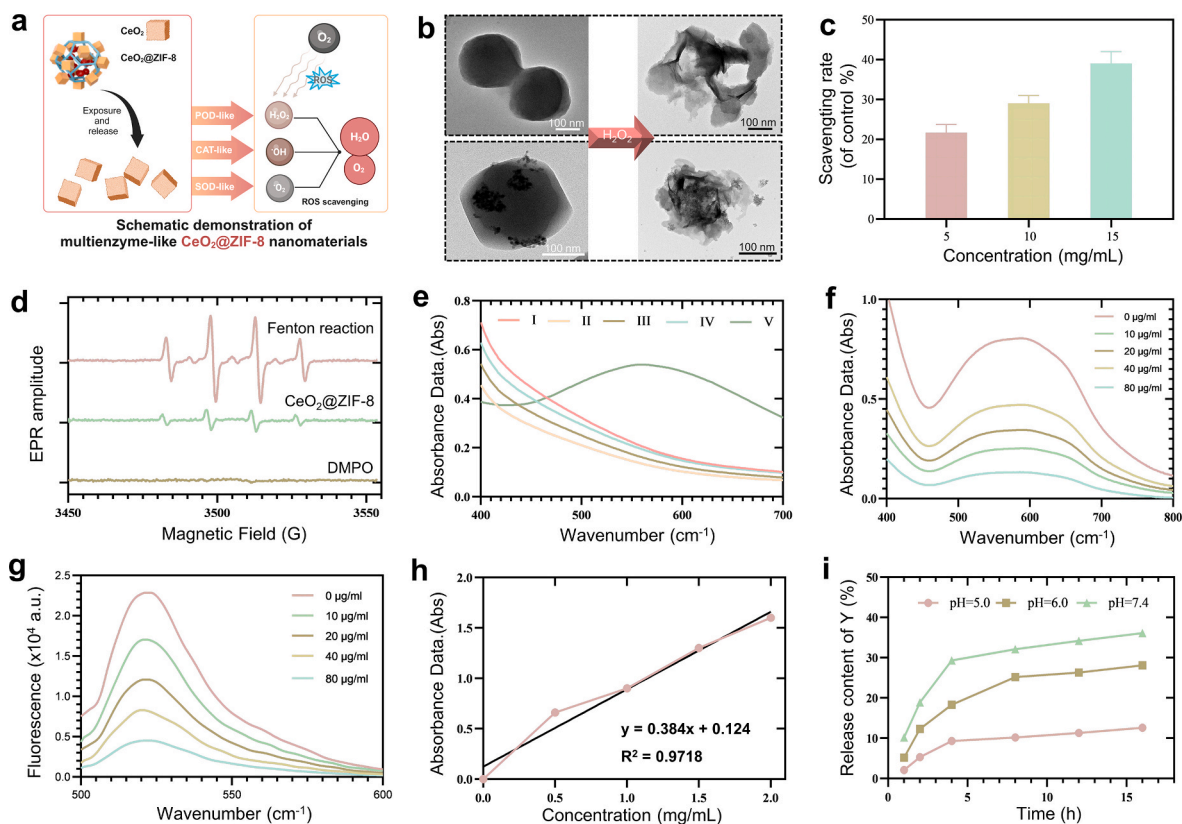


**Fig. 2.** In vitro ROS Scavenging Mechanisms of  $\text{CeO}_2@ZIF-8$  Nanoparticles. (a) Diagrammatic representation of ROS neutralization by  $\text{CeO}_2@ZIF-8$ . (b) TEM visualization of  $\text{CeO}_2@ZIF-8$  and ZIF-8 post-exposure to an aqueous 5%  $\text{H}_2\text{O}_2$  solution. (c) Assessment of *in vitro* antioxidant capabilities of  $\text{CeO}_2@ZIF-8$  via ABTS free radical scavenging assays. (d) ESR quantification of  $\bullet\text{OH}$  neutralization by  $\text{CeO}_2@ZIF-8$  (40  $\mu\text{g}/\text{mL}$ ). The Fenton reaction was initiated by the  $\text{Fe}^{2+}/\text{H}_2\text{O}_2$  system and probed using DMPO. (e) UV-vis spectral analysis of salicylic acid (SA) post-interaction with  $\bullet\text{OH}$  produced through the  $\text{Fe}^{2+}/\text{H}_2\text{O}_2$ -based Fenton reaction. I: SA +  $\text{Fe}^{2+}/\text{H}_2\text{O}_2$  +  $\text{CeO}_2@ZIF-8$  (10  $\mu\text{g}/\text{mL}$ ); II: SA +  $\text{Fe}^{2+}/\text{H}_2\text{O}_2$  +  $\text{CeO}_2@ZIF-8$  (20  $\mu\text{g}/\text{mL}$ ); III: SA +  $\text{Fe}^{2+}/\text{H}_2\text{O}_2$  +  $\text{CeO}_2@ZIF-8$  (40  $\mu\text{g}/\text{mL}$ ); IV: SA +  $\text{Fe}^{2+}/\text{H}_2\text{O}_2$  +  $\text{CeO}_2@ZIF-8$  (80  $\mu\text{g}/\text{mL}$ ); V: SA +  $\text{Fe}^{2+}$ . (f) UV-vis-NIR absorbance profiles of formazan, quantifying the SOD-mimetic activity across varying concentrations of  $\text{CeO}_2@ZIF-8$  nanoparticles. (g) Fluorescent spectral evaluation of  $\bullet\text{O}_2$  scavenging efficiency across different  $\text{CeO}_2@ZIF-8$  nanoparticle concentrations. (h) UV-vis spectral calibration curve for various Y-27632 concentrations. (i) Y-27632 release kinetics from  $\text{CeO}_2@ZIF-8$  nanoparticles under varying pH conditions.

NPs was distributed within the framework of ZIF-8. The SEM image at a higher magnification (Fig. 1c) revealed that the nanoparticles were uniform in size and strongly attached to the ZIF-8 NPs. Additionally, thorough analyses via Transmission Electron Microscopy (TEM) elucidated that the engineered nanoparticles exhibit a pronounced hollow architecture, as highlighted in Fig. 1d. Elemental mapping assessments further attested to a consistent distribution of Zn, O, and Ce constituents, as illustrated in Fig. 1e and f. Incorporating ultraviolet (UV) photosensitive properties, the gelMA gel within hydrogels, when employed in wound treatment, not only offers significant advantages in enhancing anti-inflammatory responses but also plays a pivotal role in accelerating wound healing, ensuring reduced complications and a more effective recovery process. Incorporating ultraviolet (UV) photosensitive properties, the gelMA gel within hydrogels becomes solidified after UV irradiation, as evidenced in Fig. 1g. When employed in wound treatment, this hydrogel not only offers significant advantages in enhancing anti-inflammatory responses but also plays a pivotal role in accelerating wound healing, ensuring reduced complications and a more effective recovery process. The SEM image showed that the surface of GelMA hydrogel was porous and honeycomb-like with the exterior and the interior pores interconnecting with each other (Fig. 1h). Additionally, as shown in Fig. S3, the hydrodynamic diameter of ZIF-8 and  $\text{CeO}_2@ZIF-8$  are approximately 245 nm and 283 nm respectively and the zeta potentials are  $\sim -8.17$ , and  $\sim -13.9$  eV (Fig. 1i) respectively. In the X-ray photoelectron spectroscopy (XPS) spectrum, the identifiable Ce 3d and Zn 2p peaks verify the successful amalgamation of  $\text{CeO}_2$  and ZIF-8 in the  $\text{CeO}_2@ZIF-8$  nanocomposite (Fig. 1j). Consistent Zn 2p and Ce 3d

spectra among ZIF-8,  $\text{CeO}_2$ , and  $\text{CeO}_2@ZIF-8$  provide evidence against the formation of new chemical bonds between ZIF-8 and  $\text{CeO}_2$  (Fig. 1k and l). The X-ray diffraction (XRD) pattern reveals that  $\text{CeO}_2$ , encapsulated within the ZIF-8 framework, maintains its intrinsic fluorite cubic structure (Fig. 1m). Notably, the external layer of  $\text{CeO}_2@ZIF-8$  upholds its crystalline integrity and the colloidal stability were characterized by hydrodynamic particle sizes changes in different mediums (Fig. S4). Correspondingly, the ultraviolet-visible (UV-vis) spectra showcase that  $\text{CeO}_2@ZIF-8$  aligns with the distinct absorption peak inherent to unadulterated  $\text{CeO}_2$ , further emphasizing the incorporation of  $\text{CeO}_2$  into the ZIF-8 framework (Fig. 1n).

## 2.2. Assessment of multiple enzymatic activities in vitro

Persistent inflammation and hyperglycemic conditions generate substantial reactive oxygen species (ROS) in wounds, inducing oxidative damage to cellular components. In this study, tissue engineering aims to modulate this detrimental microenvironment, thereby facilitating cell recruitment and enhancing tissue regeneration in diabetic wounds (DW) (Fig. 2a). After a 3-h exposure to a 5%  $\text{H}_2\text{O}_2$  environment, the ZIF-8 NPs disintegrated, and  $\text{CeO}_2@ZIF-8$  displayed fractures, revealing the intrinsic  $\text{CeO}_2$ , thereby elucidating the susceptibility of ZIF-8 NPs to oxidative degradation. (Fig. 2b). The antioxidant capacities of  $\text{CeO}_2@ZIF-8$  were further assessed employing the ABTS [2,2'-azinobis-(3-ethylbenzothiazoline-6-sulfonate)] free radical scavenging assays. As illustrated in Fig. 2c,  $\text{CeO}_2@ZIF-8$  suppresses the formation of ABTS free radicals in a dose-dependent manner, indicating its potent antioxidant

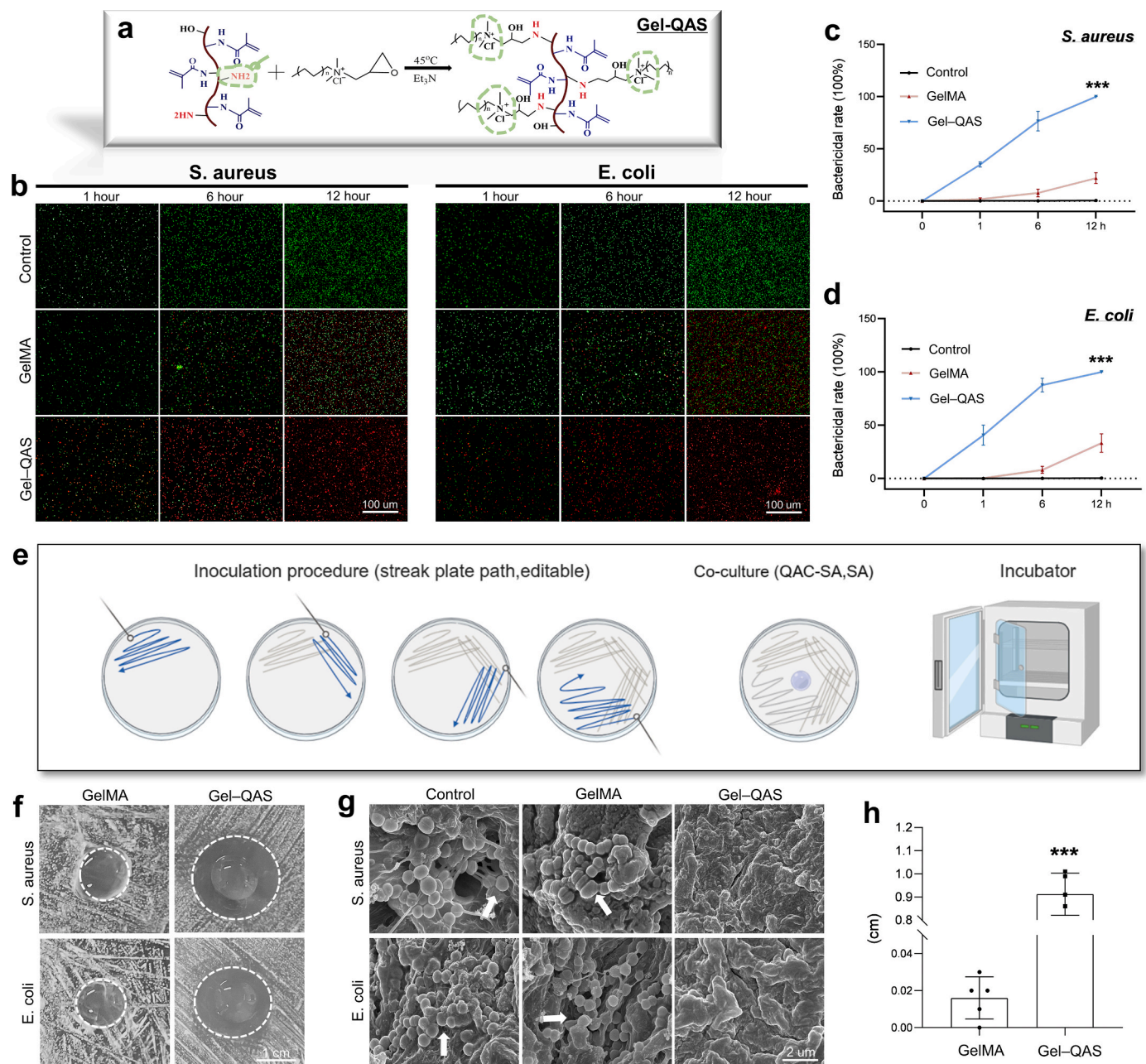


**Fig. 3.** Bactericidal capability of Gel-QAS. (a) Schematics of Gel-QAS synthesis. (b) Scheduled live/dead bacterial staining of *S. aureus* and *E. coli* cultured with Gel-QAS, and (c, d) data analyses. (e, f) Schematic illustration and results of inhibition zone assays against bacteria (*S. aureus* and *E. coli*); (h) Quantification analyses. (g) SEM observation of the remaining bacteria on skin wounds on day 3. Error bars indicate the mean  $\pm$  standard deviation, \*\*\**p* < 0.001.

capabilities. Additionally, the EPR spectra from the Fenton reaction exhibited distinct signals of DMPO-OH adducts, indicating the successful generation of the hydroxyl radical ( $\bullet$ OH) (Fig. 2d). When CeO<sub>2</sub>@ZIF-8 was introduced into the Fe<sup>2+</sup>/H<sub>2</sub>O<sub>2</sub> experimental system, the signal intensity markedly reduced, especially at the CeO<sub>2</sub>@ZIF-8 concentration of 80 μg/mL. The UV-vis spectrum displayed a characteristic peak at 520 nm, attributed to the interaction of salicylic acid (SA) with  $\bullet$ OH produced by the Fenton reaction (Fig. 2e). Notably, the absorbance at 520 nm decreased with the introduction of CeO<sub>2</sub>@ZIF-8, signifying its effective scavenging of  $\bullet$ OH radicals. This attenuation in peak intensity was dose-dependent. As shown in Fig. 2f and S5, the SOD-like activity of CeO<sub>2</sub>@ZIF-8 nanoparticles exhibited a direct correlation with their concentration, manifesting an increasing trend with concentration elevation. The ROS-quenching efficacy of CeO<sub>2</sub>@ZIF-8 nanoparticles was evaluated using 2,7-dichlorofluorescein diacetate (DCFH-DA), a

ROS-sensitive probe. A pronounced reduction in the fluorescence intensity of dichlorofluorescein (DCF) in mixtures of H<sub>2</sub>O<sub>2</sub> and CeO<sub>2</sub>@ZIF-8 underscores the nanoparticles' superior ROS elimination capacity. (Fig. 2g). From the observed results, it becomes clear that the nanostructured material exhibits enzymatic activities akin to superoxide dismutase (SOD), peroxidase (POD), and catalase (CAT), underscoring its multifunctional potential in enzymatic applications. Moreover, the standard curve could be utilized to quantitatively analyze the Y-27632 concentration to examine the release ability (Fig. S6). It was also shown in Fig. 2i that less than 10 % of the Y-27632 is found in the solution at pH 7.4 within 18 h, while approximately 25 % and 35 % of the Y-27632 was released at pH 6.0 and pH 5.0 (Fig. 2h and i).

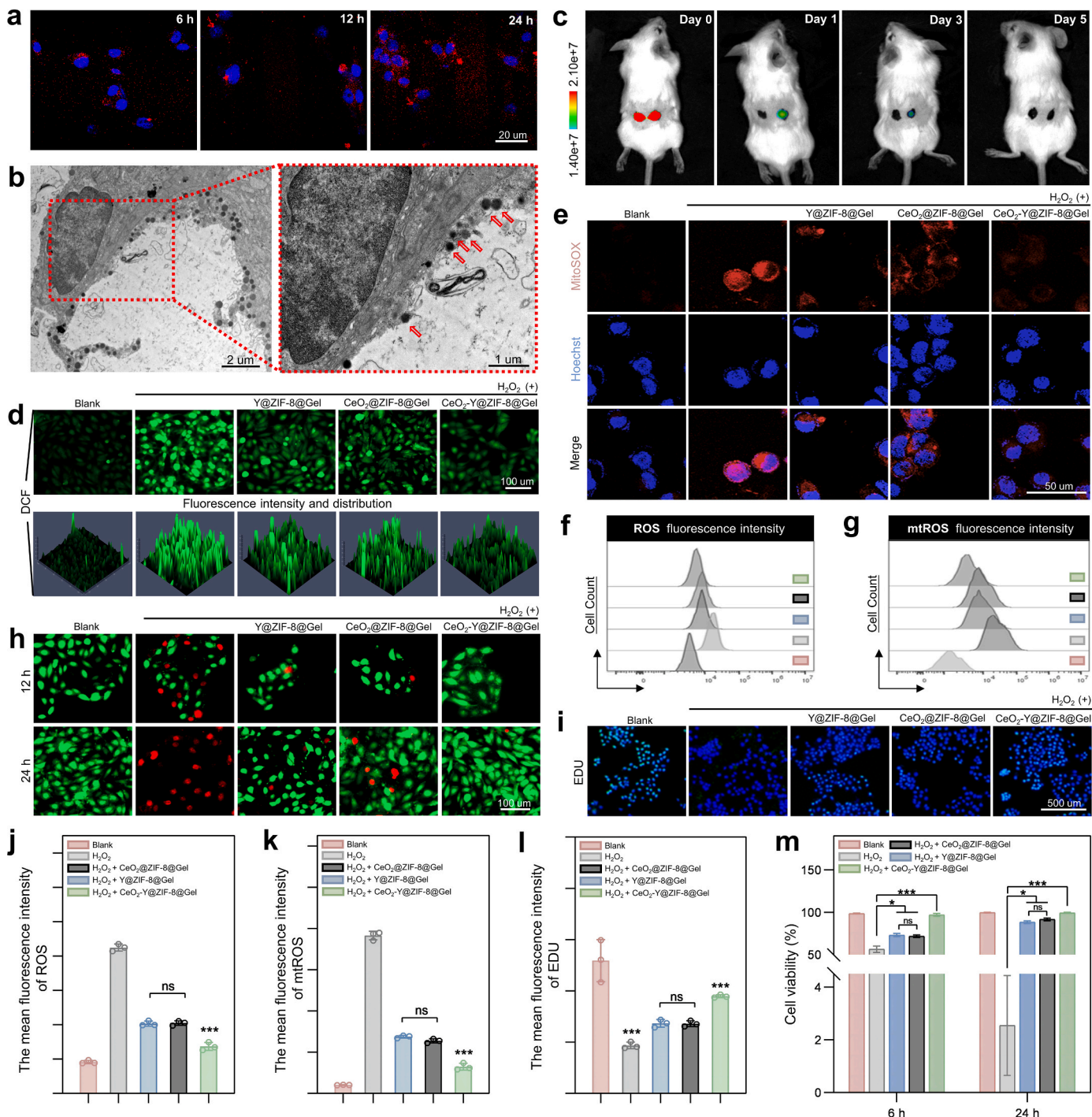


**Fig. 4.** Microenvironment improvement through antioxidative effects of CeO<sub>2</sub>-Y@ZIF-8@Gel in Endothelial cells. **(a)** CeO<sub>2</sub>-Y@ZIF-8 NPs in HUVECs were tested using immunofluorescence staining; Blue: cell nuclei stained by Hoechst 33342 dye; red: CeO<sub>2</sub>-Y@ZIF-8 NPs. **(b)** Bio-TEM of HUVEC cells uptaking nanoparticles. **(c)** Duration of the drug release *in vivo* was detected through Spectrum In-Vivo Imaging System (IVIS); left side: CeO<sub>2</sub>-Y@ZIF-8; right side: CeO<sub>2</sub>-Y@ZIF-8@Gel. **(d–e)** Confocal laser scanning microscopy (CLSM) images and **(f–g)** flow cytology of HUVEC cells for the detection of intracellular ROS, mtROS before and after incubation in H<sub>2</sub>O<sub>2</sub> with different treatment. Red: PBS; gray: H<sub>2</sub>O<sub>2</sub>; blue: H<sub>2</sub>O<sub>2</sub>+Y@ZIF-8@Gel; black: H<sub>2</sub>O<sub>2</sub>+CeO<sub>2</sub>@ZIF-8@Gel; green: H<sub>2</sub>O<sub>2</sub>+CeO<sub>2</sub>-Y@ZIF-8@Gel. **(h)** Live/dead staining of HUVECs cultured with H<sub>2</sub>O<sub>2</sub> and various hydrogels; green: fluorescence generated from the live cells; red: fluorescence generated from dead cells; **(m)** cell viability analysis. **(i)** EDU level of HUVEC and **(l)** corresponding result under the culture conditions described above. The fluorescence intensity analysis of **(j)** ROS and **(k)** mtROS in HUVEC cells. Blue: Hoechst; green: ROS; red: mtROS. Error bars indicate the mean  $\pm$  standard deviation,  $n = 3$ , n.s. = no significant, \* $p < 0.05$  and \*\*\* $p < 0.001$ .

### 2.3. Bactericidal capability of Gel-QAS

Infection caused by pathogens colonizing on the wound surface can be of considerable concern since it often leads to wound repair failure. Bacteria, as one of pathogen associated molecular pattern (PAMPs), are

potent signals that activate multiple inflammatory pathways [17]. Timely removal of the bacteria will help to inhibit inflammatory response, thereby promoting healing. Here, we proposed an antibiotic-free strategy to address the challenge of infections by using a biodegradable and cytocompatible hydrogel. The photocross-linkable



gelatin-based polymer (GelMA) was prepared and modified with cationic quaternary ammonium salt (QAS) groups via a mild and simple synthetic process (GelMA–octylQAS; abbreviation, **Gel-QAS**). As shown in Fig. 3a, the QAS groups were successfully grafted onto the gelma hydrogel. The staining results in Fig. 3b–d showed bacteria co-cultured with Gel-QAS. After 12 h, we observed that the percentage of bacteria eliminated in Gel-QAS group is over 99.99 % for both *S. aureus* and *E. coli*., while 33.27 % for *S. aureus* and 21.95 % for *E. coli*. in GelMA group. Gel-QAS group showed a significant antibacterial property in the inhibition zone assays ( $0.90 \pm 0.04$  cm; Fig. 3e, f and h). A mature biofilm was formed on the wound tissue surgically removed from diabetic patients diagnosed with *S. aureus* infection during *in vitro* culture for 2 days. After that the wound tissue was covered with Gel-QAS for 24 h. SEM images indicated excellent bactericidal capability of Gel-QAS (Fig. 3g). We believe that the Gel-QAS eliminating the pathogens in the wound is beneficial to alleviate the excessively inflammatory state in the microenvironment and interrupt the relevant immune regulation of inflammation caused by pathogens.

#### 2.4. Biocompatibility and therapeutic efficacy of CeO<sub>2</sub>-Y@ZIF-8@Gel

The wound dressing biocompatibility should be validated both *in vitro* and *in vivo*. As the transwell mode of Fig. S7, intracellular NPs were explored with the rhodamine label. Flow cytological analysis (Fig. S7) and CLSM imaging results (Fig. 4a) showed that RhB–CeO<sub>2</sub>-Y@ZIF-8 NPs could be detected intracellularly in 6 h, and the intracellular fluorescence intensity gradually increased within 24h. As shown in Fig. 4b, it was observed in the cytoplasm that the morphology of CeO<sub>2</sub>-Y@ZIF-8 NPs were becoming incompact (the enlarged image of Bio-TEM image). Further, the collected solution at different time points was observed with UV-detection, which confirmed that CeO<sub>2</sub>-Y@ZIF-8@Gel could achieve steadily long-term release for 96 h (Fig. S8). What's more, after CeO<sub>2</sub>-Y@ZIF-8@Gel being cured with light, the IVIRS images showed that fluorescent label could be detected for 5 days (Fig. 4c). It is the advantage of the CeO<sub>2</sub>-Y@ZIF-8@Gel realizing a sustained release to avoid possible cytotoxicity.

Previous studies shown that issues about NPs uptake have raised safety concerns. Therefore, the safety detection of CeO<sub>2</sub>-Y@ZIF-8@Gel is vital. On one hand, the cytotoxicity of NPs was suggested to be concentration-dependent. On the other hand, the accumulative cytotoxicity would largely vary with the particle size, surface properties, and tested cell lines. As the results presented in LDH and CCK-8 assay (Fig. S9), CeO<sub>2</sub>-Y@ZIF-8@Gel had the ideal biocompatibility without cytotoxicity. Similarly, cells co-cultured with CeO<sub>2</sub>-Y@ZIF-8@Gel exhibited a normal viability compared with control group, indicating there were no significant cytotoxicity of MSC, HaCaT, HUVEC and L929 cell lines. To validate the feasibility of CeO<sub>2</sub>-Y@ZIF-8@Gel *in vivo*, the study further evaluated its biosafety through blood biochemistry and routine toxicity analyses. In Fig. S9, hemolysis was not observed *in vitro* in blood treated with CeO<sub>2</sub>-Y@ZIF-8 NPs. To observe the degradation cycle, a certain volume of hydrogel was implanted subcutaneously in mice (Fig. S10). The hydrogel took roughly 14 days to achieve complete degradation *in vivo*, consistent with the result of biodegradation simulation with salt solution *in vitro*. The degradation rate of Gel and CeO<sub>2</sub>-Y@ZIF-8@Gel were ~98.89 % and ~99.96 % respectively, thought to be a satisfactory rate. In addition, NPs accumulation-related injury of liver was not detected after *in vivo* implantation. Briefly, we confirmed that CeO<sub>2</sub>-Y@ZIF-8@Gel has good biocompatibility without risk of circulatory accumulation. All the tests confirmed the satisfactory biocompatibility and degradation rate of CeO<sub>2</sub>-Y@ZIF-8@Gel.

It was reported that CeO<sub>2</sub>@ZIF-8 could eliminate excess ROS and convert H<sub>2</sub>O<sub>2</sub> into H<sub>2</sub>O and O<sub>2</sub>, reducing the generation of ·OH radicals, which could relieve oxidative stress and cellular injury [18]. To confirm the antioxidative therapeutic efficacy in HUVECs, flow cytology (FCM) and specific immunofluorescence analysis were first conducted to quantitatively measure the ROS and mtROS levels in HUVEC cells with

different treatments. As expected, cells incubated with CeO<sub>2</sub>-Y@ZIF-8@Gel exhibited weaker fluorescence than those treated with CeO<sub>2</sub>@ZIF-8@Gel and Y@ZIF-8@Gel (Fig. 4d and e), which could be ascribed to the alleviation of oxidative stress and cellular injury. Meanwhile, the highest fluorescence intensity was observed in the H<sub>2</sub>O<sub>2</sub> group. Moreover, the FCM analysis was conducted to further quantitatively analyze the ROS (Fig. 4f) and mtROS (Fig. 4g) production in HUVEC cells induced by different treatments, and the results were consistent with the fluorescence results (Fig. 4j and k). Along with the decrease of intracellular and mitochondrial ROS, cells proliferation was markedly enhanced. Specifically, compared with the H<sub>2</sub>O<sub>2</sub> group the proliferative activity in the Y@ZIF-8@Gel, and CeO<sub>2</sub>@ZIF-8@Gel and CeO<sub>2</sub>-Y@ZIF-8@Gel groups increased 1.37, 1.36 and 1.90-fold respectively (Fig. 4i and l). The same results were confirmed in the live/dead cell assay that the activity of HUVEC cells with CeO<sub>2</sub>-Y@ZIF-8@Gel pre-treated for 24 h reached 99.25 % (Fig. 4h and m). Combining the above results, we can conclude that the CeO<sub>2</sub>-Y@ZIF-8@Gel exhibits high efficiency in eliminating ·OH to maintain the cell viability in a hyper-oxidative environment.

#### 2.5. NLRP3 pathway-targeting ability to mediate mitochondrial function recovery

Diverse efforts have been devoted to combat inflammation through the combination of hydrogel and biomimetic nanoenzymes [19,20], yet its anti-inflammatory effect in endothelial cells and the specific mechanism in a hyperoxidative microenvironment has not been explored. To further explore the changes of endothelial cells after different treatments, CeO<sub>2</sub>-Y@ZIF-8@Gel pre-treated HUVEC cells were compared to untreated cells cultured in a hyperoxidative microenvironment via transcriptomics. A total of 756 DEGs were identified, of these 445 up-regulated and 311 down-regulated genes in PBS group compared to those with CeO<sub>2</sub>-Y@ZIF-8@Gel pre-treated group in H<sub>2</sub>O<sub>2</sub>+Glucose microenvironment (Fig. 5a). DEGs significantly enriched in immune, metabolic and complement cascade related pathways, particularly in NLRP3 pathway. TNFR2 non-canonical NF-κB pathway and TNFs binding their physiological receptors pathways were also enriched (Fig. 5b). The GO analysis showed that 71 biological processes were enriched in the up-regulated genes in PBS group vs CeO<sub>2</sub>-Y@ZIF-8@Gel pre-treated group, commonly related to immune responses and complement activation. The down-regulated genes in PBS vs CeO<sub>2</sub>-Y@ZIF-8@Gel pre-treated group clustered 39 distinct biological processes, involved in intracellular signal transduction, extracellular matrix organization, and cell communication (Fig. 5c). To further analyze the biological processes enrichment, a GSEA enrichment analysis was performed. The results implicated several immune responses significantly enriched, including humoral immune response, innate immune response, and activation of immune response (Fig. S11). In summary, the inflammation-related pathways of HUVECs in PBS group, compared to CeO<sub>2</sub>-Y@ZIF-8@Gel pre-treated group were upregulated, such as NLRP3 pathway, the active target of antioxidative therapy within a mimic diabetic wound microenvironment.

Emerging evidence highlights that ROCK plays an important role in the process of mitochondrial oxidative stress and ROCK inhibitor (ROCKi) can relieve mitochondrial oxidative stress and protect mitochondrial function [21,22]. Previous studies reported the usage of the ROCKi in the treatment of diseases characterized by mitochondrial dysfunction [23]. Its therapeutic effects in the model of severe mitochondrial dysfunction *in vitro* [24] may lead to the development of much-needed disease-modifying therapeutics for mitochondrial dysfunction-related disorders. As a kind of ROCKi, the potential of Y-27632 has been proved to enhance endotheliocyte proliferation and migration, and protect against apoptosis [25–27]. However, the anti-inflammatory role of Y-27632 in repairing diabetic wounds remains unexplored. We tested the target protein binding sites between Y-27632 and ROCK. The bonds formed in ALA-103, ALA-215, ASP-160, LEU-205,

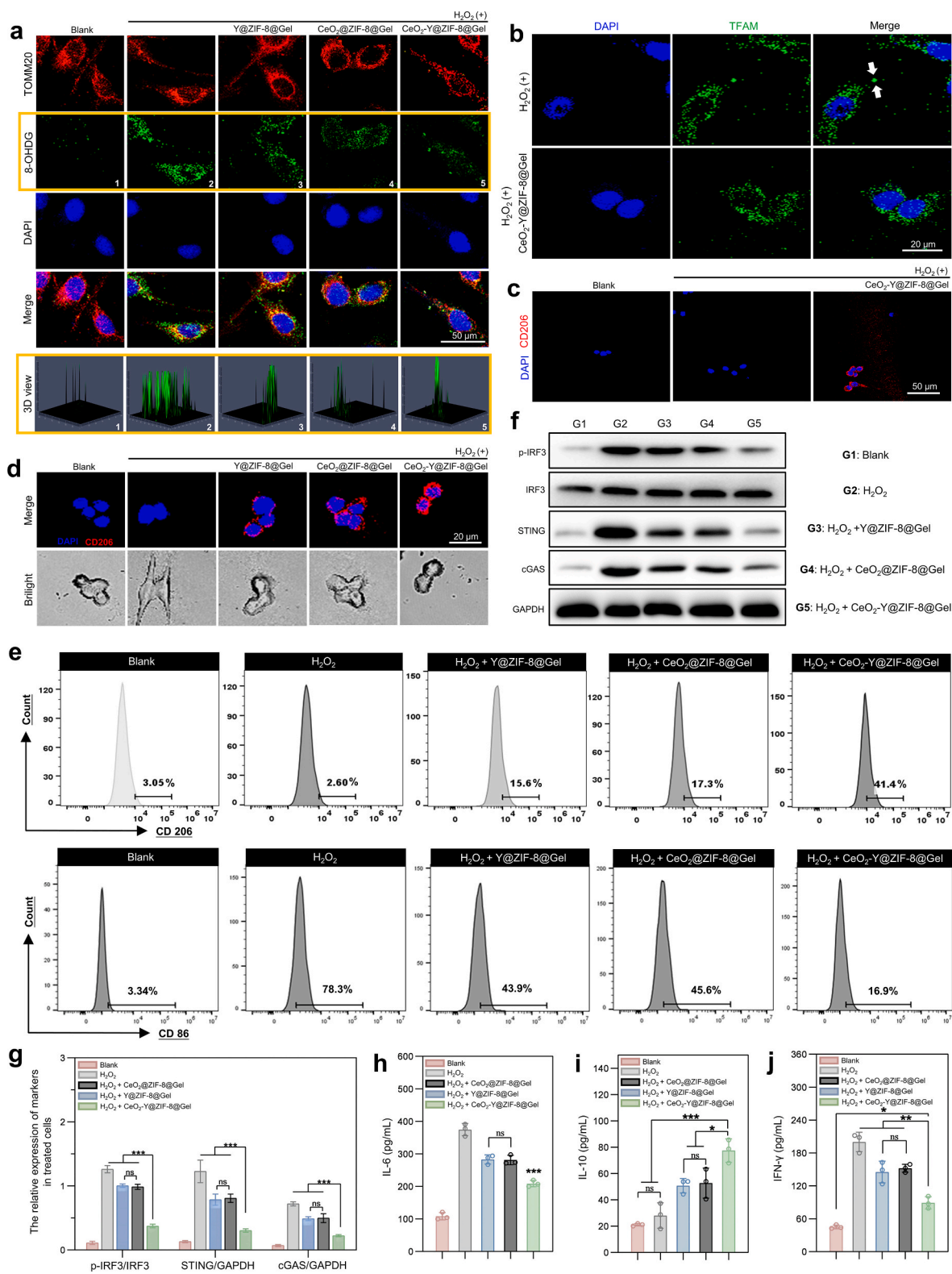


**Fig. 6.** CeO<sub>2</sub>-Y@ZIF-8@Gel reduces the activation of cGAS-STING pathway in macrophages to induce M2 phenotype polarization. (a) CLSM images of 8-OHdG in mitochondria of HUVEC cells. (b) CLSM images of TFAM in HUVECs. White arrow within the red region indicated the extracellular overflow of Ox-damaged DNA. (c, d) CLSM images and (e) flow cytology of CD206 and CD86 in macrophage cells. (f) Western blotting and (g) data analysis for proteins of the cGAS/STING signaling pathway. (h–j) ELISA analysis of IL-6, IL-10 and IFN-γ from the macrophage cells cultivated with H<sub>2</sub>O<sub>2</sub>. Error bars indicate the mean ± standard deviation, n = 3, n.s. = no significant, \*p < 0.05, \*\*p < 0.01 and \*\*\*p < 0.001.

VAL-90, GLY83 and GLU154 of ROCK at the binding pocket (Fig. 5d), indicating that the regulations in HUVECs cells were caused by Y-27632 directly binding and inhibiting ROCK to regulate the mitochondrial function. Then, the bio-TEM was used to further validate the effect of CeO<sub>2</sub>-Y@ZIF-8@Gel on damaged mitochondria. The mitochondrial morphology of HUVECs in the Blank group was normal, while that in the CeO<sub>2</sub>-Y@ZIF-8@Gel group were closer to normal compared with the H<sub>2</sub>O<sub>2</sub> group (Fig. 5e, white arrows). Finally, the mitochondrial function, which is vital for cells to maintain metabolism [28] and proliferation [29], was observed via mitochondrial permeability transition pore (mPTP) and mitochondrial membrane potential ( $\Delta\Psi$ m). Physiological opening of the mPTP is indispensable for maintaining mitochondrial function and cell homeostasis [30], and excessive opening of mPTP is considered to activate pathophysiological processes by causing cellular and mitochondrial ion and oxidative imbalances [31]. The CLSM and FCM results showed that the opening rate of the mPTP following treatment with CeO<sub>2</sub>-Y@ZIF-8@Gel was lowest than any other group co-cultured with H<sub>2</sub>O<sub>2</sub>, indicating that the mPTP could close in time (Fig. 5f–S12 and S13). Calcein selectively accumulates within mitochondria, showing fluorescence which is quenched by CoCl<sub>2</sub> when calcein escapes outside the mitochondria due to excessive opening of the mPTP [32]. In addition, as an important biomarker for evaluating mitochondrial function, the  $\Delta\Psi$ m can be inferred from the red/green fluorescence intensity ratio detected by JC-1 staining and FCM. We observed that HUVECs co-cultured with CeO<sub>2</sub>-Y@ZIF-8@Gel showed stronger red fluorescence (JC-1 aggregates) inside the mitochondria, a result consistent with the normal mitochondrial potential, while stronger green fluorescence (JC-1 monomer) and weaker red fluorescence were produced in CeO<sub>2</sub>@ZIF-8@Gel and Y@ZIF-8@Gel group CeO<sub>2</sub>-Y@ZIF-8@Gel, which is consistent with mitochondrial damage (Fig. 5g, h and S14). The above results exhibited the protective role of CeO<sub>2</sub>-Y@ZIF-8@Gel in relieving the mitochondrial oxidative damage and rehabilitating the mitochondrial function.

We then analyzed whether the CeO<sub>2</sub>-Y@ZIF-8@Gel could be exploited as a pathway regulator for diabetes-mediated inflammation in wound repair. NLRP-3 can be induced by mitochondria-mediated apoptosis, and promote the increase of chemokines such as IL-1 $\beta$ , accelerate the infiltration of peripheral M $\Phi$ s and other inflammatory cells into the wound tissue, produce a large number of proinflammatory cytokines resulting in a locally hyper-inflammatory state [33]. Specifically, NLRP3 inflammasome activation is accompanied with the aggregation and cleavage of pro-Caspase-1, which then generates the mature, structurally intact Caspase-1, leading to pro-IL-1 $\beta$  and pro-IL-18 lysis to generate the inflammatory cytokines IL-1 $\beta$  and IL-18 [34,35]. Subsequently, we validated the association between the inflammation-related NLRP3 pathway and CeO<sub>2</sub>-Y@ZIF-8@Gel in its protection of mitochondria (downregulated in oxidative environment; Fig. 5a–c). First, western blotting assays confirmed that NLRP3 expression in CeO<sub>2</sub>-Y@ZIF-8@Gel group appeared low (Fig. 5i and S15) and second, proinflammatory factors (IL-1 $\beta$  and IL-18) were less produced in cells pre-treated with CeO<sub>2</sub>-Y@ZIF-8@Gel as shown in ELISA results (Fig. S16). NLRP3 inflammasome-mediated IL-1 $\beta$  and IL-18 are the critical regulators of vascular sprouting in skin repair [36]. These findings are consistent with earlier reports demonstrating that chronic wound is closely associated with NF- $\kappa$ B/NLRP-3 inflammatory pathway [37]. CeO<sub>2</sub>-Y@ZIF-8@Gel effectively targets cells with overexpression of the NLRP3 pathway to inhibit inflammation and reduce cellular oxidative damage (Fig. 5j). Additionally, through the amelioration of mitochondrial function, CeO<sub>2</sub>-Y@ZIF-8@Gel regulates the NLRP3 pathway to achieve anti-inflammation. In this part, the evidences of CeO<sub>2</sub>-Y@ZIF-8@Gel, exploited as a pathway regulator for diabetes-mediated inflammation in wound repair, were presented.

## 2.6. Regulation on M1 to M2 transition based on the cGAS–STING pathway activated by escaped Ox-mtDNA from endotheliocyte

Early studies supported that macrophage(M $\Phi$ ) and endotheliocyte (EC) are two important types of cells with distinct but interconnected roles in tissue homeostasis and wound repair. In the M $\Phi$ –EC interplay, EC is a critical regulator for M $\Phi$ s to determine their fate of activation, polarization and differentiation in immune response and inflammation [38]. In turn, EC integrity was supported by M $\Phi$  through regulating EC metabolism and function, vascular growth and sprouting in angiogenesis and regeneration [39]. As the results shown in Fig. 5, oxidative stress may activate the NLRP3 pathway, which is relative to mitochondrial DNA (mtDNA). Notably, previous studies have indicated that mtDNA is more susceptible to the attack by mitochondrial-generated mtROS without histone protection, leading to the oxidative damage of mtDNA and mitochondrial dysfunction [40]. When macrophages are exposed to metabolic danger signals, mitochondria play a key role in a “two-step” activation of NLRP3 inflammasome, as mtDNA synthesized during “priming” couples with mtROS generated during “activation” to produce Ox-mtDNA, which enters the cytosol to trigger NLRP3 inflammasome activation [41]. However, the mechanisms of CeO<sub>2</sub>-Y@ZIF-8@Gel impacting M $\Phi$ -EC niches in living organisms to improve homeostasis for diabetic wounds still remains obscure. We further detected the regulation effect of the CeO<sub>2</sub>-Y@ZIF-8@Gel in macrophage (M $\Phi$ ) phenotype *in vitro*. HUVECs were incubated in PBS or H<sub>2</sub>O<sub>2</sub> for a day after pre-cultured with Y@ZIF-8@Gel, CeO<sub>2</sub>@ZIF-8@Gel and CeO<sub>2</sub>-Y@ZIF-8@Gel for 24 h. M $\Phi$  ( $1 \times 10^6$ /mL) were seeded into the confocal dishes and incubated at 37 °C for 48 h with supernatants of HUVEC cells treated under various co-culture conditions as described above. Interestingly, the CLSM images showed that cells uptaking CeO<sub>2</sub>-Y@ZIF-8 had obviously strengthened resistance to H<sub>2</sub>O<sub>2</sub> damages and decreased amount of Ox-mtDNA (8-OHdG; Fig. 6a and S17). Extracellular leakage of Ox-mtDNA in HUVEC was weakly observed by TFAM immunofluorescence staining (Fig. 6b). The mtDNA binds to TFAM introducing a specific curvature to form a mitochondrial transcription factor, potentially activates cGAS [42].

Next, we verified the vital role of the released mitochondrial DNA in microenvironment inflammation. As previous studies mentioned, DNA damages can be sensed by immunocytes and activates the STING/interferon I pathway, resulting in enhanced cross-priming capacity and tumor-specific CD8<sup>+</sup> T cell activation. It is notable that M $\Phi$  is a crucial immunocyte in skin inflammation and has important association with endotheliocytes, so we further investigated whether CeO<sub>2</sub>-Y@ZIF-8@Gel could reduce HUVEC mtDNA release to less activate the M $\Phi$ 's cGAS-STING pathway in a synergistic manner. M0 phenotype macrophages were placed in Blank, H<sub>2</sub>O<sub>2</sub> and CeO<sub>2</sub>@ZIF-8@Gel groups respectively and co-cultured for 24h, immunofluorescence revealed that the macrophages in the H<sub>2</sub>O<sub>2</sub> group tended to be M1, while in the CeO<sub>2</sub>-Y@ZIF-8@Gel group M2 (Fig. 6c and S18). The result revealed that CeO<sub>2</sub>-Y@ZIF-8@Gel may contribute to M $\Phi$  polarization toward the anti-inflammatory phenotype. Then, CeO<sub>2</sub>-Y@ZIF-8@Gel regulating the interaction of HUVECs and M $\Phi$ s in the inflammatory microenvironment was further explored. After the HUVECs being pre-treated with the three differentiated nanomaterials for 24h, the supernatants were collected and added to the PBS and H<sub>2</sub>O<sub>2</sub> groups to observe macrophage morphological changes respectively. As expected, supernatant of HUVECs co-cultured with CeO<sub>2</sub>-Y@ZIF-8@Gel reversed the M1 to M2 transition (Fig. 6d, e and S19). Western blotting assay also confirmed that the cGAS/STING pathway of M $\Phi$  was remarkably decreased in the CeO<sub>2</sub>-Y@ZIF-8@Gel group (Fig. 6f and g). In Fig. 6h–j, the expression of the pro-inflammatory factors IFN- $\gamma$  and IL-6 secreted by M1 cells, were significantly decreased in the CeO<sub>2</sub>-Y@ZIF-8@Gel group, along with a correspondingly increased expression of the anti-inflammatory factor IL-10 secreted by M2 cells. The above evidences unveiled that as Ox-mtDNA cytophagy decreased, the cGAS-STING pathway-dependent M1 maturation was inhibited by CeO<sub>2</sub>-Y@ZIF-8@Gel and macrophage

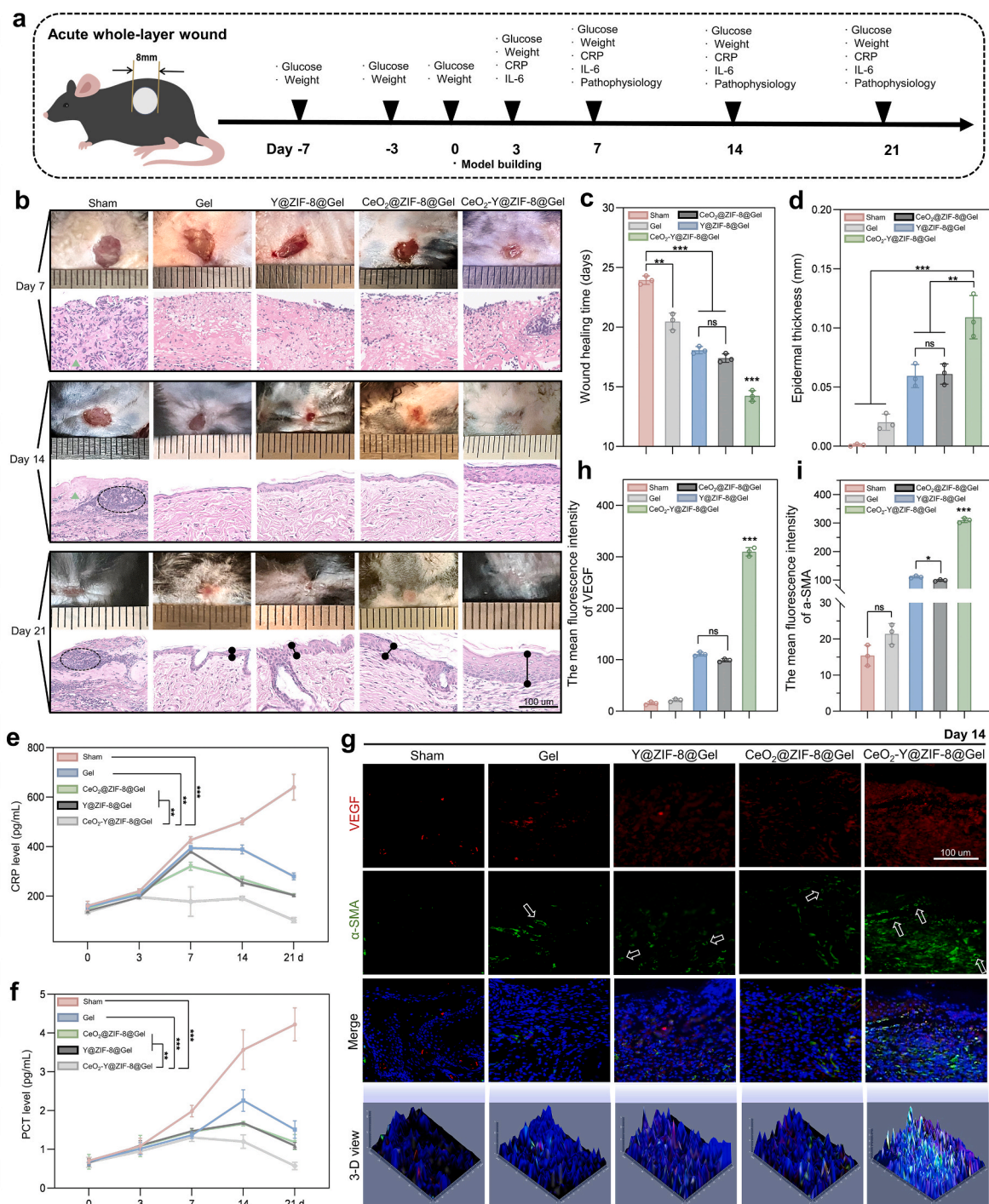


**Fig. 7.** CeO<sub>2</sub>-Y@ZIF-8@Gel accelerates wound healing by promoting vascularization *in vivo*. (a) Schematic illustration of animal experiments. (b) Photographs of infected wounds and corresponding images of H&E staining, (c) days required to achieve wound-healing in the five groups with different treatments, and (d) Statistical analysis of the thickness of the nascent epidermal layer on day 21. The black circles indicate the neutrophile granulocytes aggregation; the green arrows indicate the edematous tissue; point lines represent re-epithelialization areas. (e) CRP levels and (f) PCT levels of the mice subjected to different treatments at scheduled time points. (g) Immunofluorescence staining of α-SMA (green), VEGF (red) and CD-31 (red) at the wound site during different phases of wound healing. (h–i) Corresponding quantitative analysis of VEGF and α-SMA expression. Error bars indicate the mean ± standard deviation, n = 3, \*p < 0.05, \*\*p < 0.01 and \*\*\*p < 0.001.

polarization to M2 phenotype increased. Specifically, though treated with CeO<sub>2</sub>-Y@ZIF-8@Gel, the Ox-mtDNA was either repaired or less escaped within mitochondria via mPTP-dependent channels to inhibit cytosolic NLRP3 inflammasome (a key sensor and effector of tissue damage) initiation and IL-1β secretion leading MΦ polarization.

Meanwhile, cGAS-STING pathway activation in MΦ was reduced as less mtDNA was uptaken and MΦ ultimately exhibited polarization to the anti-inflammatory phenotype.

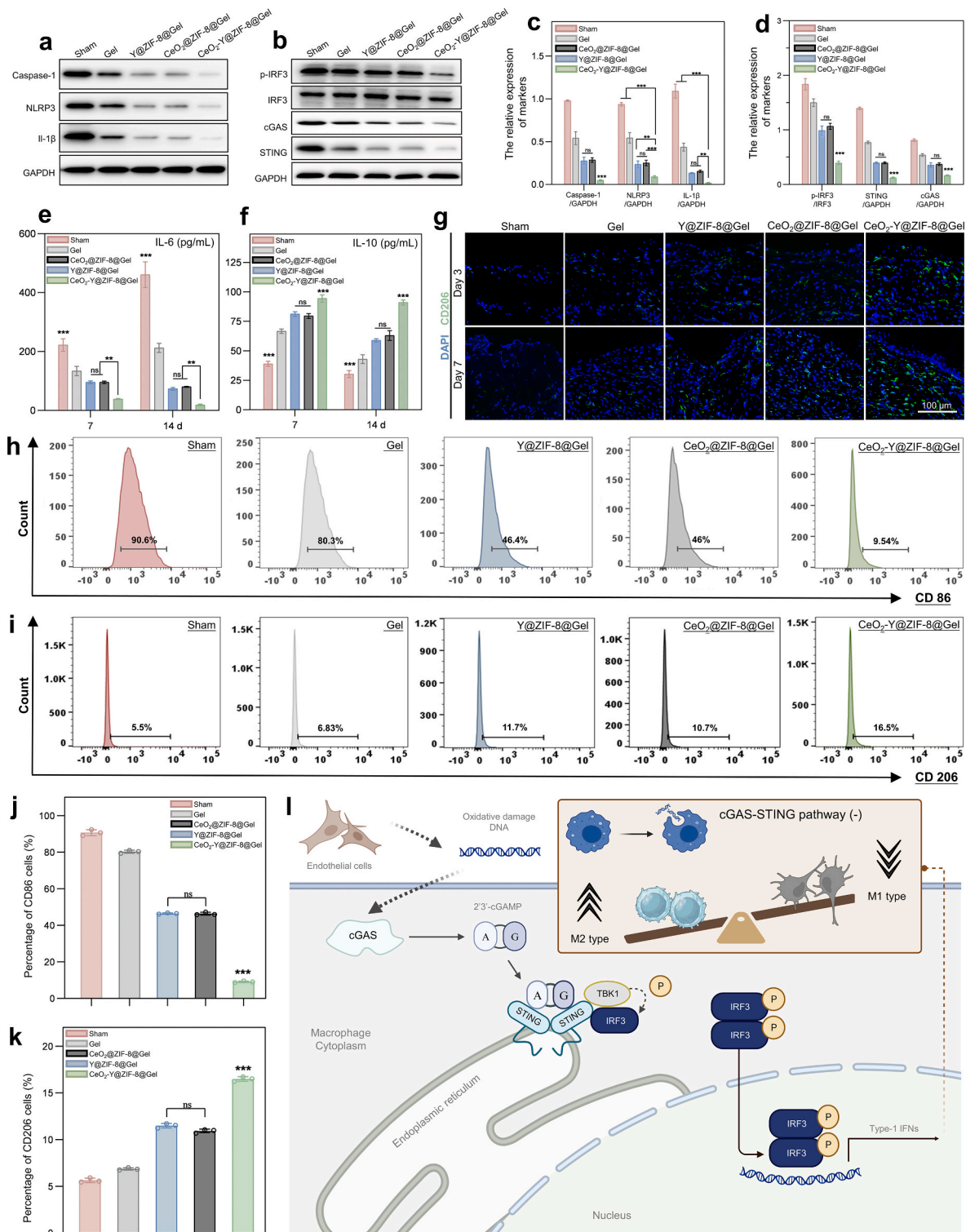


**Fig. 8.** CeO<sub>2</sub>-Y@ZIF-8@Gel inhibits inflammatory pathways and regulates macrophage polarization pathways *in vivo* to enhanced immunoregulation. (a, c) Western blot and analysis of proteins in NLRP3 signal pathway in skin tissues isolated from mice wounds treated with PBS (Sham), Gel, Y@ZIF-8@Gel, CeO<sub>2</sub>@ZIF-8@Gel and CeO<sub>2</sub>-Y@ZIF-8@Gel respectively. (b, d) Western blot and analysis of proteins in cGAS–STING signal pathway. (e, f) ELISA analysis of IL-6 and IL-10 from the wound tissue on day 7 and 14 after injury. (g) Immunofluorescence staining of CD206 (M2 marker) at day 3 and 7 after injury. (h, i) The flow cytology of nascent tissue for CD86 (marker of M1 macrophage) and CD206 (marker of M2 macrophage), and (j, k) corresponding analyses. (l) Illustration of CeO<sub>2</sub>-Y@ZIF-8@Gel can induce M2 phenotype polarization via reducing NLRP3-mediated mitochondrial DNA damage and down-regulate the cGAS/STING pathway in macrophages activated by OxtDNA. Error bars indicate the mean  $\pm$  standard deviation, n = 3, \*\*p < 0.01, \*\*\*p < 0.001, n.s. = no significance.

### 2.7. *In vivo* anti-inflammatory effect and promoting wound repair via facilitating vascularization

Encouraged by the satisfactory antioxidative effect *in vitro*, the oxidative stress resistance effect of CeO<sub>2</sub>@ZIF-8@Gel was further evaluated *in vivo*. A schematic of the animal experiments is shown in Fig. 7a. The Gel, Y@ZIF-8@Gel, CeO<sub>2</sub>@ZIF-8@Gel and CeO<sub>2</sub>-Y@ZIF-8@Gel dressings were used in the infected diabetic wounds. We recorded the progress of wound healing by taking pictures and measuring the changing wound size. Compared with Sham, Gel, Y@ZIF-8@Gel and CeO<sub>2</sub>@ZIF-8@Gel groups which took about 24, 20, 18 and 17 days respectively to achieve wound healing, the CeO<sub>2</sub>-Y@ZIF-8@Gel group boasted the fastest wound healing with an average of 14 days (Fig. 7b and c). Its efficacy in promoting wound healing was assessed using H&E staining on day 7, 14 and 21, the CeO<sub>2</sub>-Y@ZIF-8@Gel-treated wound tissue exhibited the fastest healing, followed by those from the Y@ZIF-8@Gel and CeO<sub>2</sub>@ZIF-8@Gel groups. The wounds using antibacterial hydrogels (Gel) significantly promoted basal tissue regeneration compared with the Sham group (Fig. 7b and d). The persistent non-healing wound of Sham group showed significant neutrophil accumulation (black circle area) and tissue edema (green triangles). Mice of Sham, Gel, Y@ZIF-8@Gel and CeO<sub>2</sub>@ZIF-8@Gel groups showed poor appetite and massive glycogen depletion, but consistently met the criteria of diabetic mice, indicating the local regulatory effect of CeO<sub>2</sub>-Y@ZIF-8@Gel (Fig. S20), and evidencing control of the local infection can help to improve the systemic nutritional status. Meanwhile, the infection index (CRP, PCT) in the mice were significantly decreased (Fig. 7e and f), indicating the CeO<sub>2</sub>-Y@ZIF-8@Gel has an optimal control of inflammation and promotes wound healing.

Vascularization difficulty due to persistent inflammation is considered a key issue in non-healing diabetic wounds. We subsequently examined the degree of vascularization of the new tissue in different groups. First, the levels of vascular endothelial growth factor VEGF (Fig. 7g) were quantified via immunofluorescence staining. Notably, we found that CeO<sub>2</sub>-Y@ZIF-8@Gel increased the expression of VEGF on day 14, consistent with visual observation that no significant angiogenesis could be observed in the Sham and Gel groups. Although we observed angiogenesis in the CeO<sub>2</sub>@ZIF-8@Gel and Y@ZIF-8@Gel groups, there was no significant difference between them (Fig. 7h). It is worth mentioning that fibroblasts participate in the later stage of wound repair to reconstruct dermal tissue [43]. According to the co-stained fluorescent results of fibroblast marker  $\alpha$ -SMA, the regenerated skin tissues treated with CeO<sub>2</sub>-Y@ZIF-8@Gel was much more ordered in basal layer (Fig. 7g and i). This suggested the involvement of fibroblasts in tissue reconstruction was also regulated by CeO<sub>2</sub>-Y@ZIF-8@Gel, but the further exploration of fibroblast-related repair mechanism is still on the way.

After verifying the therapeutic effect of CeO<sub>2</sub>-Y@ZIF-8@Gel for wound repair *in vivo*, the expression of cGAS-STING and NLRP3 pathways in skin tissues that suffered from diabetes was inspected. Consistent with the *in vitro* experiments, western bolt assay detected a downregulation of NLRP3 pathway and cGAS/STING pathway activation in newborn tissue on day 7 of the CeO<sub>2</sub>-Y@ZIF-8@Gel wound coverage (Fig. 8a–d). In Fig. 8e and f, the expression of the pro-inflammatory factor IL-6 was significantly decreased and that of the anti-inflammatory factor IL-10 increased in the wound treated with CeO<sub>2</sub>-Y@ZIF-8@Gel. In addition, in identification of macrophages, lower expression of CD86 (M1 specific marker) and higher expression of CD206 (M2 specific marker) were found compared to other groups (Fig. 8g–k). *In vivo* experiments verified that CeO<sub>2</sub>-Y@ZIF-8@Gel could reduce NLRP3-mediated mitochondrial DNA damage and down-regulate the cGAS/STING pathway in macrophages activated by Ox-mtDNA, resulting in M2 phenotype polarization (Fig. 8l). In conclusion, diabetic wounds treated with CeO<sub>2</sub>-Y@ZIF-8@Gel heals faster may be attributed to the elimination of infection, acceleration of vascularization and amelioration of the inflammatory microenvironment.

### 3. Conclusion

To promote the healing of infected diabetic wounds (DW), the study designed CeO<sub>2</sub>-Y@ZIF-8@Gel, a novel biomimetic hydrogel that integrates antibacterial and anti-inflammatory properties with the adaptability to wounds. CeO<sub>2</sub>-Y@ZIF-8@Gel continuously releases the nanoenzyme CeO<sub>2</sub> with superoxide dismutase (SOD) and catalase (CAT) activity to catalyze the dismutation of superoxide anion radical (O<sup>2-</sup>) and the decomposition of hydrogen peroxide into oxygen and water, as well as the molecule drug of Y-27632 to repair Ox-mtDNA and accelerate DW healing. Its therapeutic effects can be confirmed in controlling inflammation, promoting early vascularization, and boosting extracellular matrix (ECM) reconstruction. Firstly, CeO<sub>2</sub>-Y@ZIF-8@Gel is confirmed to be a promising nanocomposite for regulating the immune microenvironment, for it downregulates the inflammation-related signaling pathways (NLRP-3/Caspase-1/IL-1 $\beta$ ) activated by continuous accumulation of ROS, relieves mitochondria-mediated apoptosis and lowers chemokines to inhibit the infiltration of peripheral macrophages. Additionally, reduced PAMPs and lowered leakage of oxidative mitochondrial damage DNA (Ox-mtDNA) (damage-related pattern molecules, DAMPs) decrease the cGAS-STING pathway activation. Subsequently M $\Phi$ s transform into the anti-inflammatory M2 phenotype to produce anti-inflammatory factors ameliorating the inflammatory microenvironment. This study presents the versatile nanocomposite which modulates multiple mechanisms in signal transduction in wound healing and provides a strategy to achieve the immunoregulation between endothelial cells and macrophages for early vascularization and regeneration, which would add to the existing non-surgical treatments for diabetic wounds.

### Ethics approval

All animal experimental protocols were approved by the Animal Research Ethics Committee of the Fourth Medical Center of Chinese PLA General Hospital (approval number: 82072169, 82272279), and complied with the rules of the specific pathogen-free animal laboratory. All methods followed the guidelines for animal subject care and use outlined in the Guide for the Care and Use of Laboratory Animals (Institute of Laboratory Animal Resources, National Academy of Sciences, Bethesda, MD, USA).

### CRedit authorship contribution statement

**Shan He:** Writing – review & editing, Writing – original draft, Visualization, Validation, Software, Resources, Methodology, Investigation, Formal analysis, Data curation, Conceptualization. **Zhenhao Li:** Writing – review & editing, Visualization, Validation, Software, Resources, Funding acquisition, Formal analysis, Data curation, Conceptualization. **Lu Wang:** Visualization, Validation, Software, Investigation, Formal analysis, Data curation. **Nannan Yao:** Validation, Resources, Investigation, Formal analysis, Data curation. **Huangding Wen:** Visualization, Resources, Investigation, Formal analysis, Data curation. **Huageng Yuan:** Writing – review & editing, Visualization. **Jiatao Zhang:** Writing – review & editing, Visualization, Supervision, Resources, Project administration, Formal analysis, Data curation, Conceptualization. **Zhiqing Li:** Supervision, Project administration, Investigation, Funding acquisition, Data curation, Conceptualization. **Chuanan Shen:** Writing – review & editing, Visualization, Supervision, Resources, Project administration, Methodology, Investigation, Funding acquisition, Conceptualization.

### Declaration of competing interest

The authors declare no competing interests.

## Acknowledgements

This research was supported by the Program of National Natural Science Foundation of China (C.S; Grant Number 82272279, 82072169), Guangdong Basic and Applied Basic Research Foundation (Z.L; Grant Number 2414050005704), Science and Technology Planning Project of Guangdong Province (Z.L; Grant Number 2017A020215042) and College Students' Innovative Entrepreneurial Training Plan Program (S.H; Grant Number 202312121032).

## Appendix A. Supplementary data

Supplementary data to this article can be found online at <https://doi.org/10.1016/j.bioactmat.2024.01.005>.

## References

- N. Cho, J. Shaw, S. Karuranga, et al., IDF Diabetes Atlas: global estimates of diabetes prevalence for 2017 and projections for 2045, *Diabetes Res. Clin. Pract.* 138 (2018) 271–281.
- D. Armstrong, T. Tan, A. Boulton, et al., Diabetic foot ulcers: a review, *JAMA* 330 (1) (2023) 62–75.
- S. Crunkhorn, Promoting efferocytosis heals diabetic wounds, *Nat. Rev. Drug Discov.* 21 (7) (2022) 491.
- R. Numan, K. Harding, P. Martin, Clinical challenges of chronic wounds: searching for an optimal animal model to recapitulate their complexity, *Disease models & mechanisms* 7 (11) (2014) 1205–1213.
- J. Wada, H. Makino, Innate immunity in diabetes and diabetic nephropathy, *Nat. Rev. Nephrol.* 12 (1) (2016) 13–26.
- L. Billingham, J. Stoolman, K. Vasani, et al., Mitochondrial electron transport chain is necessary for NLRP3 inflammasome activation, *Nat. Immunol.* 23 (5) (2022) 692–704.
- D. Lv, X. Cao, L. Zhong, et al., Targeting phenylpyruvate restrains excessive NLRP3 inflammasome activation and pathological inflammation in diabetic wound healing, *Cell reports Medicine* 4 (8) (2023) 101129.
- Y. Zhao, Q. Wang, S. Yan, et al., Bletilla striata polysaccharide promotes diabetic wound healing through inhibition of the NLRP3 inflammasome, *Front. Pharmacol.* 12 (2021) 659215.
- T. Lazarov, S. Juarez-Carreño, N. Cox, et al., Physiology and diseases of tissue-resident macrophages, *Nature* 618 (7966) (2023) 698–707.
- K. Hu, N. Kuhn, T. Courau, et al., Transcriptional space-time mapping identifies concerted immune and stromal cell patterns and gene programs in wound healing and cancer, *Cell Stem Cell* 30 (6) (2023) 885, 903 e810.
- X. Zhang, J. Gan, L. Fan, et al., Bioinspired adaptable indwelling microneedles for treatment of diabetic ulcers, *Advanced materials (Deerfield Beach, Fla)* 35 (23) (2023) e2210903.
- A. Ablasser, Z. Chen, cGAS in action: expanding roles in immunity and inflammation, *Science (New York, NY)* 363 (6431) (2019).
- G. Barber, STING: infection, inflammation and cancer, *Nat. Rev. Immunol.* 15 (12) (2015) 760–770.
- K. Garland, T. Sheehy, J. Wilson, Chemical and biomolecular strategies for STING pathway activation in cancer immunotherapy, *Chem. Rev.* 122 (6) (2022) 5977–6039.
- J. Park, H. Kang, C. Park, et al., A crucial role of ROCK for alleviation of senescence-associated phenotype, *Exp. Gerontol.* 106 (2018) 8–15.
- L. Atar-Froyman, A. Sharon, E. Weiss, et al., Anti-biofilm properties of wound dressing incorporating nonrelease polycationic antimicrobials, *Biomaterials* 46 (2015) 141–148.
- A. Adamczyk, M. Leicaj, M. Fabiano, et al., Extracellular vesicles from human plasma dampen inflammation and promote tissue repair functions in macrophages, *J. Extracell. Vesicles* 12 (6) (2023) e12331.
- C. Liu, L. Gui, J.J. Zheng, et al., Intrinsic strain-mediated ultrathin ceria nanoantioxidant, *J. Am. Chem. Soc.* 145 (34) (2023 Aug 30) 19086–19097.
- Y. Zhao, S. Song, D. Wang, et al., Nanozyme-reinforced hydrogel as a H<sub>2</sub>O<sub>2</sub>-driven oxygen generator for enhancing prosthetic interface osseointegration in rheumatoid arthritis therapy, *Nat. Commun.* 13 (1) (2022) 6758.
- M. He, Z. Wang, H. Yang, et al., Multi-functional bio-HJzyme: revolutionizing diabetic skin regeneration with its glucose-unlocked sterilization and programmed anti-inflammatory effects, *Adv. Sci.* 10 (21) (2023) e2300986.
- A.J. Kruppa, C. Kishi-Itakura, T.A. Masters, et al., Myosin VI-dependent actin cages encapsulate parkin-positive damaged mitochondria, *Dev. Cell* 44 (4) (2018) 484, 499.e486.
- J. Shi, X. Wu, M. Surma, et al., Distinct roles for ROCK1 and ROCK2 in the regulation of cell detachment, *Cell Death Dis.* 4 (2) (2013) e483.
- N. Moskal, V. Riccio, M. Bashkurov, et al., ROCK inhibitors upregulate the neuroprotective Parkin-mediated mitophagy pathway, *Nat. Commun.* 11 (1) (2020) 88.
- H. Kang, J. Park, K. Choi, et al., Chemical screening identifies ROCK as a target for recovering mitochondrial function in Hutchinson-Gilford progeria syndrome, *Aging Cell* 16 (3) (2017) 541–550.
- G.S. Peh, K. Adnan, B.L. George, et al., The effects of Rho-associated kinase inhibitor Y-27632 on primary human corneal endothelial cells propagated using a dual media approach, *Sci. Rep.* 5 (2015) 9167.
- N. Okumura, N. Koizumi, E.P. Kay, et al., The ROCK inhibitor eye drop accelerates corneal endothelium wound healing, *Invest. Ophthalmol. Vis. Sci.* 54 (4) (2013) 2493–2502.
- L.R. Kopecky, B.W.H. Lee, M.T. Coroneo, A systematic review on the effects of ROCK inhibitors on proliferation and/or differentiation in human somatic stem cells: a hypothesis that ROCK inhibitors support corneal endothelial healing via acting on the limbal stem cell niche, *Ocul. Surf.* 27 (2023) 16–29.
- Z. Hu, D. Wang, J. Gong, et al., MSCs deliver hypoxia-treated mitochondria reprogramming acinar metabolism to alleviate severe acute pancreatitis injury, *Adv. Sci.* 10 (25) (2023) e2207691.
- T. Miettinen, M. Björklund, Mitochondrial function and cell size: an allometric relationship, *Trends Cell Biol.* 27 (6) (2017) 393–402.
- X. Wang, H. Du, S. Shao, et al., Cyclophilin D deficiency attenuates mitochondrial perturbation and ameliorates hepatic steatosis, *Hepatology* 68 (1) (2018) 62–77.
- E.H. Park, Y.J. Kim, N. Yamabe, et al., Stereospecific anticancer effects of ginsenoside Rg3 epimers isolated from heat-processed American ginseng on human gastric cancer cell, *Journal of Ginseng research* 38 (1) (2014) 22–27.
- G. Morciano, N. Naumova, P. Kowalewski, et al., The mitochondrial permeability transition pore: an evolving concept critical for cell life and death, *Biol. Rev. Camb. Phil. Soc.* 96 (6) (2021) 2489–2521.
- J. Chen, Z.J. Chen, PtdIns4P on dispersed trans-Golgi network mediates NLRP3 inflammasome activation, *Nature* 564 (7734) (2018) 71–76.
- D. Zheng, W. Chen, T. Chen, et al., Hydrogen Ion Capturing Hydrogel Microspheres for Reversing Inflammation, *Advanced Materials, Deerfield Beach, Fla*, 2023 e2306105.
- I. Afonina, Z. Zhong, M. Karin, et al., Limiting inflammation—the negative regulation of NF- $\kappa$ B and the NLRP3 inflammasome, *Nat. Immunol.* 18 (8) (2017) 861–869.
- S. Willenborg, T. Lucas, G. van Loo, et al., CCR2 recruits an inflammatory macrophage subpopulation critical for angiogenesis in tissue repair, *Blood* 120 (3) (2012) 613–625.
- J. Li, X. Wang, Z. Yao, et al., NLRP3-Dependent crosstalk between pyroptotic macrophage and senescent cell orchestrates trauma-induced heterotopic ossification during aberrant wound healing, *Adv. Sci.* 10 (19) (2023) e2207383.
- G.E. Hernandez, M.L. Iruela-Arispe, The many flavors of monocyte/macrophage–endothelial cell interactions, *Curr. Opin. Hematol.* 27 (3) (2020) 181–189.
- H. Hong, X.Y. Tian, The role of macrophages in vascular repair and regeneration after ischemic injury, *Int. J. Mol. Sci.* 21 (17) (2020).
- H. Jiang, Y. Guo, C. Wei, et al., Nanocatalytic innate immunity activation by mitochondrial DNA oxidative damage for tumor-specific therapy, *Adv. Mater.* 33 (20) (2021) e2008065.
- Z. Zhong, S. Liang, E. Sanchez-Lopez, et al., New mitochondrial DNA synthesis enables NLRP3 inflammasome activation, *Nature* 560 (7717) (2018) 198–203.
- L. Andreeva, B. Hiller, D. Kostrewa, et al., cGAS senses long and HMGB/TFAM-bound U-turn DNA by forming protein-DNA ladders, *Nature* 549 (7672) (2017) 394–398.
- S. He, H. Wu, J. Huang, et al., 3-D tissue-engineered epidermis against human primary keratinocytes apoptosis via relieving mitochondrial oxidative stress in wound healing, *J. Tissue Eng.* 14 (2023) 20417314231163168, <https://doi.org/10.1177/20417314231163168>.